$Ni_{2-x}Mn_xP$ nanoparticles as earth-abundant pre-catalysts for electrochemical water oxidation

Fatemeh Aghabozorgi, S. Sameera Perera, Stephanie L. Brock*

Department of Chemistry, Wayne State University, Detroit, MI USA 48221

*sbrock@chem.wayne.edu

Abstract: Establishing efficient catalysts based on earth-abundant elements is critical for large scale adoption of electrocatalytic water splitting. In this work, the synthesis of $Ni_{2-x}Mn_xP$ nanoparticles with different ratios of Ni to Mn is described and these phases are evaluated as pre-catalysts for the electrocatalytic oxygen evolution reaction (OER) process. Using arrested precipitation techniques, it was possible to incorporate up to 75% Mn into Ni_2P ($x \leq 1.5$), which represents a greater solubility for Mn relative to previously studied $Fe_{2-x}Mn_xP$ ($x \leq 0.9$) and $Co_{2-x}Mn_xP$ ($x \leq 1.4$) systems. Electrocatalytic OER activity assessment of the $Ni_{2-x}Mn_xP$ system (pH = 14) as a function of x revealed maximum activity for x=1. Faradaic efficiency was calculated as 96.6%, indicating high selectivity of the NiMnP-derived catalyst towards the OER process. After an initial drop in the current density (ca 20% over 1 h) during controlled potential electrolysis (CPE) measurements the current density remains constant over the remainder of the 15 h test, suggesting reasonable stability. The X-ray photoelectron spectroscopy data collected on samples before and after catalysis indicate the NiMnP pre-catalyst is becoming oxidized during the OER process, losing phosphate and forming the Ni-Mn oxide/hydroxide presumed catalyst *in situ*. Compared to the most active compositions in $Fe_{2-x}Mn_xP$ ($x \leq 0.9$) and $Co_{2-x}Mn_xP$ ($x \leq 1.4$), the NiMnP pre-catalyst resulted in the highest OER activity with a geometric overpotential of 280.0 mV at 10 mA/cm^2 relative to 302.5 mV for CoMnP and 350.0 mV for $Fe_{1.1}Mn_{0.9}P$. The relative activity can be correlated to electronegativity differences between Mn and M (M = Fe, Co, Ni), which governs the extent of oxo-mediated charge transfer between Mn and M, and hence, the activity of the catalyst.

INTRODUCTION

A promising route to produce green hydrogen is electrocatalytic water splitting coupled with renewable sources of electrical energy. However, electrocatalytic water splitting faces significant challenges due to the high kinetic energy barriers associated with the water oxidation[1] (oxygen evolution reaction, OER) process responsible for delivering the electrons and protons needed for water reduction (hydrogen evolution reaction, HER). RuO_2 and IrO_2 are state-of-the-art electrocatalysts, but comprise scarce and expensive metals. Large-scale adoption of electrocatalytic water splitting is predicated on discovering robust OER catalysts made from earth-abundant elements.[2-3] Among different materials evaluated, transition metal phosphides (TMPs) such as Ni_2P, which are established hydrotreating catalysts that are also excellent HER catalysts,[4, 5] have recently been shown to exhibit promising activity towards the OER process, despite the fact that OER is fundamentally incompatible with phosphide chemistry. Work in this area suggests that phosphides are pre-catalysts for OER that are activated upon surface oxidation, with phosphide converting to phosphate, which subsequently undergoes dissolution.[6-8] In fact, the native conductivity of the metallic phosphide is purported to play an important role in increasing the activity of formed oxide/hydroxide sites (relative to bulk phase oxides/hydroxides) by electron transfer from the “core” conducting phosphide to the active “shell” oxide responsible for catalyzing the OER process.[9] Among transition metal phosphides, there is abundant data suggesting that incorporation of a secondary metal enhances the catalytic activity of the *in situ* formed catalyst [10, 11] and our group has studied the incorporation of Mn into binary phosphides Co_2P and Fe_2P. Notably, $Co_{2-x}Mn_xP$ nanoparticles with Mn incorporation up to 1.4 are more active than Co_2P, and their composition-dependent OER electrocatalytic activity study reveals that the most active phase arises from x=1, CoMnP, with an overpotential of 330 mV at 10 mA/cm^2 vs 370 mV for Co_2P nanoparticles under the same conditions.[6] Likewise, Mn incorporation into Fe_2P can be achieved with a maximum Mn uptake of x=0.9, reducing the overpotential of the resultant catalysts from 590 mV for Fe_2P to 350 mV at 10 mA/cm^2.[7]

Examples of Mn incorporation into Ni_2P nanoparticles are limited. In 2018, Tsang and co-workers reported a series of “doped” ca. 8 nm diameter discrete Ni_2P particles prepared from mixtures of Ni acetate with acetates of Fe, Co, Mn, and Mo (1:1 by metals basis) in a solvent system comprising oleylamine (reductant), trioctylphosphine (phosphorus source), and trioctylphosphine oxide at 300 ºC. However, uptake of Mn was limited to ca. 5% on a metals basis, and incorporation resulted in a dramatic increase in overpotential relative to the undoped Ni_2P case.[12] More recently (2020) Peter and co-workers[13] reported the synthesis of $Ni_{2-x}Mn_xP$ with maximum Mn incorporation of 0.5 using a solvothermal method. The reaction, which involved treatment of Mn and Ni salts with red phosphorus, produced large aggregated structures with a size of 80-90 nm. In contrast to the Tsang paper, where no shifts in the diffraction pattern was noted, the Peter paper shows diffraction pattern shifts in peak position to lower 2ϴ, consistent with Vegard's Law, at low Mn incorporation ($x \leq 0.2$) but at higher Mn concentrations, peaks shift to higher 2ϴ, which they attributed to tensile strain. Electrocatalytic OER (in base) and HER (in acid) processes indicated that with increase in the Mn content up to x=0.5, both OER and HER activities increase. An overpotential of 109 mV at 10 mV/cm^2 was reported for acidic HER and an overpotential of 265 mV at 20 mA/cm^2 was reported for basic OER in $Ni_{1.5}Mn_{0.5}P$, which was reported to be the most active species in both HER and OER processes. Inspired by these studies, we focus on the synthesis of crystalline monodisperse $Ni_{2-x}Mn_xP$ nanoparticles with Mn incorporation up to and beyond x=0.5, probing the solubility of Mn into the Ni_2P system, and considering the effect of Mn uptake in the OER process.

EXPERIMENTAL SECTION

Reagents: Anhydrous nickel (II) bis(acetylacetonate) [$Ni(acac)_2$, 95%] was obtained from Alfa Aesar, dimanganese decacarbonyl [$Mn_2(CO)_{10}$, 98%], dicobalt octacarbonyl [$Co_2(CO)_8$, 90%] Trioctylphosphine (TOP) (97%), and 1-Octadecene (ODE) (90%) were purchased from Sigma-Aldrich and stored in a glovebox. Oleylamine (OAm) (70%) was purchased from Sigma-Aldrich, hexane (Certified ACS grade) from Fisher Chemical, ethanol (200 proof) from Decon Laboratories, and isopropanol (99.5%) from Honeywell Laboratories Plus. KOH (≥85%, pellets), Nitric acid Omni Trace (HNO_3) and sulfuric acid (H_2SO_4) Omni Trace were purchased from Sigma-Aldrich. Nafion (5%, LQ-1105) was purchased from Fisher Scientific. OAm is dried over activated molecular sieves: type 3Å, 8-12 mesh. All other chemicals were used as received.

Synthesis of $Ni_{2-x}Mn_xP$ nanoparticles: Scheme 1 shows the synthesis procedure for $Ni_{2-x}Mn_xP$ nanoparticles (x=0.5). 1.5 mmol of $Ni(acac)_2$ is dissolved in 10.0 mL of ODE and 4.0 ml of dried OAm in a 200 mL Schlenk flask with a condenser. This system is degassed at 110 °C for 20 min and then purged with Ar at 220 ℃ for 30 min. At the same time, 0.25 mmol of $Mn_2(CO)_{10}$ is added to 2.0 ml of dried OAm and 5.0 ml of ODE in a glovebox and capped with a septum. Then, the solution is heated at 80 °C for 1 hour to dissolve the $Mn_2(CO)_{10}$. The Mn_2CO_{10} solution was withdrawn with a syringe from the flask and injected through the condenser of the Ni-containing solution and the temperature is maintained at 220 °C for 30 min. Any changes in the color from black to dark red, green or yellow is an indication of oxidation of manganese, which is correlated with a lower Mn uptake. The temperature is then increased to 350 ℃ for 3h. Due to competitive formation of Mn_xO_y with adventitious O_2, Mn incorporation of x=1.0 and 1.5 requires excess Mn precursor to be employed. For x=1, the **Scheme 1** process is used but with 0.5 mmol of $Ni(acac)_2$ and 0.75 mmol $Mn_2(CO)_{10}$. For x=1.5, 0.90 mmol $Mn_2(CO)_{10}$ is first injected into 0.20 mmol of $Ni(acac)_2$ followed by a second injection of 0.25 mmol $Mn_2(CO)_{10}$ (**Scheme S1**). In addition, the maximum Mn incorporation (x=1.5) requires a 50:50 mixture of ODE and octylether.

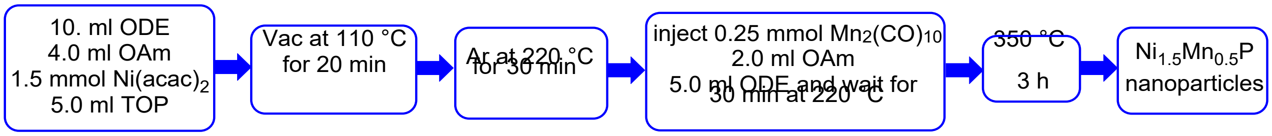

Scheme 1. Flowchart showing the synthesis of $Ni_{2-x}Mn_xP$ nanoparticles for x=0.5. (ODE: Octadecene, OAm: Oleylamine, TOP: Trioctylphosphine).

Safety warning: *This procedure uses trioctylphosphine at elevated temperature, which can potentially produce toxic and flammable PH_3 gas. All reactions were performed under inert atmosphere on a standard Schlenk line mounted in a hood.*

Purification of $Ni_{2-x}Mn_xP$ nanoparticles: For the purification, nanoparticles are first isolated using hexane and ethanol. Hexane is used for dispersing nanoparticles and ethanol is applied for their precipitation. As shown in **Scheme 2**, after collecting nanoparticles, 5 ml of hexane is added to disperse the nanoparticles and then, a mixture of oleic acid and distilled water (5 ml oleic acid to 5 ml water) is added to the nanoparticles followed by sonication for 15 min. After completing the sonication, two layers settle out; the top layer is black (manganese nickel phosphide nanoparticles dispersed in hexane). The lower layer is grayish and includes manganese oxides in water. The black hexane layer (containing $Ni_{2-x}Mn_xP$) is separated from the grayish water layer (containing Mn_xO_y).

The oleic acid/water treatment is performed 3 more times. Finally, $Ni_{2-x}Mn_xP$ nanoparticles are collected by precipitating with ethanol and drying under vacuum.

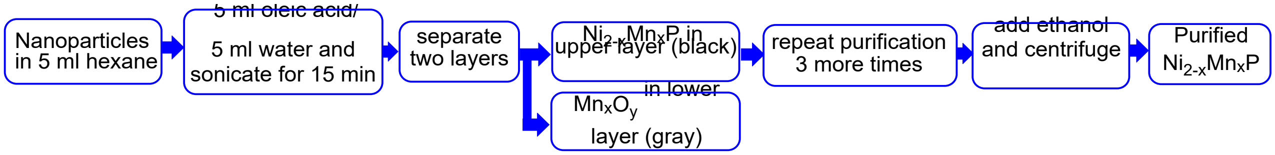

Scheme 2. Process for the purification of $Ni_{2-x}Mn_xP$ nanoparticles using oleic acid/water treatment.

Synthesis of Ni_2P nanoparticles: Ni_2P nanoparticles are synthesized using a modification of a previous method.[14] 0.59 g of $Ni(acac)_2$, 6.0 ml of dried OAm, 15.0 ml of octylether and 2.0 ml of TOP is added to a 200 ml Schlenk flask. This mixture is degassed at 110 °C for 20 min followed by purging with Ar for 90 min at 230 °C. After that, 3.0 ml of TOP is injected in to the solution and then the temperature is increased to 350 °C for 3 h. The reaction is naturally cooled to room temperature, and nanoparticles are isolated and purified by dispersing in chloroform and precipitating with ethanol. This purification process is repeated once.

Synthesis of CoMnP nanoparticles: CoMnP nanoparticles are synthesized by modification of a previous method.[6] 10.0 ml ODE is mixed with 1.5 ml dried OAm in a 200 ml Schlenk flask and degassed at 110℃ for 20 min following with purging with Ar at 230℃ for 30 min. In the glovebox, 0.75 mmol of $Mn_2(CO)_{10}$ and 0.75 mmol of $Co_2(CO)_8$ are added to 7.0 ml of ODE in a 100 ml round bottom flask, and the flask is capped with a septum. The solution is slowly heated to 80℃ for 1h to facilitate the dissolution. This solution is added through the condenser into the one neck flask containing 10.0 ml ODE and 1.5 ml of OAm at 230°C, and the temperature was maintained for 20 min. After that, 3.0 ml of TOP is added to the solution by injecting through the condenser and the temperature is increased to 350°C and maintained for 3 h. Synthesized nanoparticles are collected and purified three times using hexane (dispersion) and ethanol (precipitation) followed by centrifugation.

Ink Preparation: As-synthesized nanoparticles were dried under vacuum and then 50.0 mg of dried nanoparticles was mixed with 25.0 mg of Ketjen-300J carbon (C) in hexane and ultrasonicated for 30 min to produce carbon supported-nanoparticles (C-NP). Particles were subsequently isolated by adding ethanol followed by centrifugation. C-NPs were then annealed under 5% H_2/Ar at 400℃ to remove the ligands from the surface of the particles. The ink was prepared by mixing 15.0 mg of annealed C-NPs in 2.0 ml of ethanol, 1.0 ml of nanopure water, 1.0 ml of isopropanol, and 1.0 ml of a 5 wt % Nafion solution, followed by sonication for 30 min.

Powder X-ray Diffraction (PXRD). Powder X-ray diffraction measurements were conducted on a Bruker D2 Phaser X-ray diffractometer using the Kα line (λ = 0.15406 nm) of a Cu source operated at 10 mA and 30 kV. Samples were deposited using drop casting on a zero-background quartz holder. Data were collected in the 2θ range from 20° to 70° with a step size of 0.02° and a scan rate of 0.5 s per step. Eva v3.1 software was used to process the PXRD patterns and then the peaks were compared to the reference powder diffraction files (PDFs) from the ICDD. Scherrer crystallite sizes have been calculated using the Scherrer equation ($D = \frac{K\lambda}{\beta Cos\theta}$) by fitting peak positions; β and θ are the full width at half maximum (FWHM) and Bragg angle, respectively. A K value of 0.9 was used.[15]

Transmission Electron Microscopy (TEM), Energy-dispersive X-ray Spectroscopy (EDS), and Scanning Transmission Electron Microscopy (STEM): Electron microscopy and energy dispersive spectroscopy (EDS) were performed using a JEOL 2010 electron microscope operated at a voltage of 200 kV and a beam current of 107−108 μA with a coupled EDS detector (EDAX Inc.). The images were captured using Amtv600 software provided by the Advanced Microscopy Techniques Corp. A Thermo Fisher Talos F200X G2 scanning transmission electron microscope was used to collect STEM elemental mapping data. The instrument was operated at 200 kV and equipped with a high angle annular dark field (HAADF) and EDAX detectors. Samples for TEM and STEM/EDS mapping have been prepared by dispersing the nanoparticles in hexane followed by sonication for 30 min. Then a drop of the solution was deposited on the surface of a carbon-coated 200 mesh Cu grid, followed by drying in air. Average particle sizes have been calculated for ca 200 particles using NIS software on the images taken from TEM/STEM.

X-ray Photoelectron Spectroscopy (XPS): High-resolution C1s, O1s, Mn2p, and P2p spectra were recorded using a Thermo Scientific Nexsa X-ray Photoelectron Spectrometer (XPS) with a hemispherical analyzer and monochromatic Al K*α* (1486.7 eV) source. Due to the strong overlap between the Ni2$p_{3/2}$ core line and the F KLL Auger line (from fluorine in the Nafion polymer), Ni2p spectra of inks were collected using an Omicron XPS/UPS system with a Mg K*α* (1253.7 eV) source and an Argus detector.[16] All the spectra were collected using a 40 eV pass-energy, 0.1 eV energy step size, and 100 ms/step dwell time. Recorded spectra were analyzed using Thermo Avantage® v5.9922 software to extract the spectra. The C1s peak at 284.8 eV is used as a charge reference to determine the binding energies (BEs).

Inductively Coupled Plasma Mass Spectrometry (ICP-MS). An Agilent 7700 ICP-MS instrument was employed to measure the concentration of Ni, Mn, and P dissolved in the electrolyte post-catalysis. The KOH solution was collected after the stability test and 2 ml of this solution is diluted to a volume of 15 ml with 2 M HNO_3. A series of external standards including 0, 5, 10, 25, 50, 100, 150, 200 ppb of standard solutions of Ni, Mn, and P were prepared for calibration (acidified with 2 M HNO_3 to a volume of 15 ml).

Electrochemical Measurements. Cyclic voltammograms (CV) have been collected using an EC epsilon potentiostat equipped with a rotating disc electrode (RDE). A standard three-electrode setup with Ag/AgCl reference electrode and Pt wire auxiliary electrode was employed. The glassy carbon working electrode has a surface area of 0.07 cm^2. 10.0 µl of the ink (catalytic loading of 0.284 mg/cm^2_{geo}) was deposited on the glassy carbon electrode surface. OER measurements were done in 1 M KOH solution by running 20 CV cycles to activate the catalyst and then collecting CVs at a scan rate of 10 mV/s with the RDE at 1600 rpm. Potentials were measured versus Ag/AgCl and then converted to the reversible hydrogen electrode (RHE) by using the equation $E(RHE)=E_{Ag/AgCl}+0.197+0.059\times pH$ (pH=14 in 1M KOH). The iR compensation option from the Epsilon software has been used to determine the resistivity of the solution and then corrections have been applied based on the equation $E(RHE) = E_{Ag/AgCl} + (0.197+0.059 \times pH) - iR$. Double-layer capacitances (C_{dl}) were measured by running CV scans using the same abovementioned experiment in the non-faradaic region at scan rates of 10, 25, 50, 75, and 100 mV/s within the potential range of ±50 mV of the open-circuit potential (OCP). C_{dl} values were found from the slope of the current-density vs. scan-rate plots, and electrochemical surface area data were calculated by dividing the double layer capacitance by the specific capacitance (C_{dl}/C_s). A C_s value of 0.04 mF/cm^2 was selected based on typically recorded values in basic media.[2, 17] The computed surface area was also calculated based on the average particle size (supporting information).

Bulk Electrolysis and Faradaic Efficiency. Bulk electrolysis was done using a custom-built H-type cell with a Pt coil as the auxiliary electrode and Ag/AgCl as the reference electrode in 1M KOH. A carbon cloth with the area of 1cm^2 was heated in the oven at 400 °C for 2 h to remove residual organic material. Then, 140.0 μL of the ink was drop- cast on the carbon cloth followed by drying under an IR lamp. A GOW-MAC series 400 gas chromatograph equipped with a TCD detector was used to determine the amount of O_2 gas from the head space of the H-type cell. Carrier and internal standard gases are Helium and Nitrogen, respectively. The faradaic efficiency was obtained by calculating the theoretical amount of O_2 based on the charge consumption, relative to the amount measured by GC.

RESULTS

Synthesis and characterization. $Ni_{2-x}Mn_xP$ nanoparticles ($x\leq1.5$) were synthesized using an arrested precipitation technique and characterized by PXRD and TEM as shown in **Figures 1 and 2**. Product compositions were determined from TEM/EDS (**Figures S1-S4, Table S1**) and this information was used to tune the synthesis for reproducible targeting of three compositions (x=0.5, 1.0, 1.5), as shown in **Table 1**. In the two-step synthesis, the Ni-P amorphous phase is formed first from reaction of $Ni(acac)_2$ with trioctylphosphine (TOP) in octadecene (ODE) and oleylamine (OAm) at 220 °C, and then $Mn_2(CO)_{10}$ is added in a second step, followed by heating at 350 °C to make the $Ni_{2-x}Mn_xP$ nanoparticles (see **Scheme 1**). The addition of zerovalent Mn as a second step is critical to the success of the reaction; attempts to prepare $Ni_{2-x}Mn_xP$ by direct mixing of reagents resulted in formation of Ni_2P and Mn_xO_y (**Figure S5**). Indeed, because of the oxophilicity of Mn, formation of Mn_xO_y as a byproduct is a common occurrence, particularly for higher values of x. Accordingly, excess Mn is included in the synthesis for x>0.5 and a purification strategy using aqueous oleic acid to extract Mn_xO_y was developed (**Figure S6**). Comparing the PXRD of the nanoparticles before (**Figure S6(b) before**) and after (**Figure S6(b) after**) treatment with oleic acid and water demonstrates that peaks for

Mn_xO_y at 35° and 59° are absent after the treatment. Incorporation of x=1.5 further required a second injection of Mn and a change in the solvent system from ODE to a mixture of ODE/octylether (**Scheme S1**). Specifically, in single solvent systems, ODE enabled incorporation of x only up to 1.2 as probed by TEM/EDS (**Figure S7, S8**), whereas the use of octylether enabled incorporation up to x = 1.5, but the particles were very small (~3.6 nm by TEM) and the samples were compositionally heterogeneous with respect to Ni (**Figure S9, S10**). By combining the two solvents (50:50), it was possible to prepare compositionally uniform particles with x = 1.5 that have sizes comparable to the other compositions (~4.9 nm by TEM).

As can be seen from PXRD for the purified $Ni_{2-x}Mn_xP$ nanoparticles **(Figure 1a)**, the peaks are shifted to the left, or to lower 2θ, with the increase in the Mn incorporation. This shift is indicative of an expansion of the unit cell as the Mn, which has a larger atomic radius than Ni, is incorporated into the Ni_2P crystal structure. The graph of changing d-spacing for the (111) reflection peak versus the experimentally-determined Mn content shows a nearly linear behavior with an R^2 value of 0.983 (**Figure 1b**), consistent with Vegard's law, and suggesting solid-solution formation is occurring. Note that the reported value for bulk NiMnP falls on the best fit line.[18] In addition, for relatively large concentrations of Mn, (x≥1) the PXRD peaks become broad; increasing breadth suggests a decrease in crystallite size and/or possible disorder. The Scherrer equation was applied to non-overlapping peaks (111, 201, 210), and the crystallite sizes of the corresponding reflections and the averages were computed (**Table 1**). The Scherrer sizes of $Ni_{2-x}Mn_xP$ nanoparticles are consistent with an initial increase in crystallite size upon incorporation of Mn (from 6.4 nm for x = 0 to 7.9 nm for x = 0.5) followed by a decrease in the crystallite size with more Mn incorporation (to 4.5 nm for x = 1 and 3.3 nm for x = 1.5).

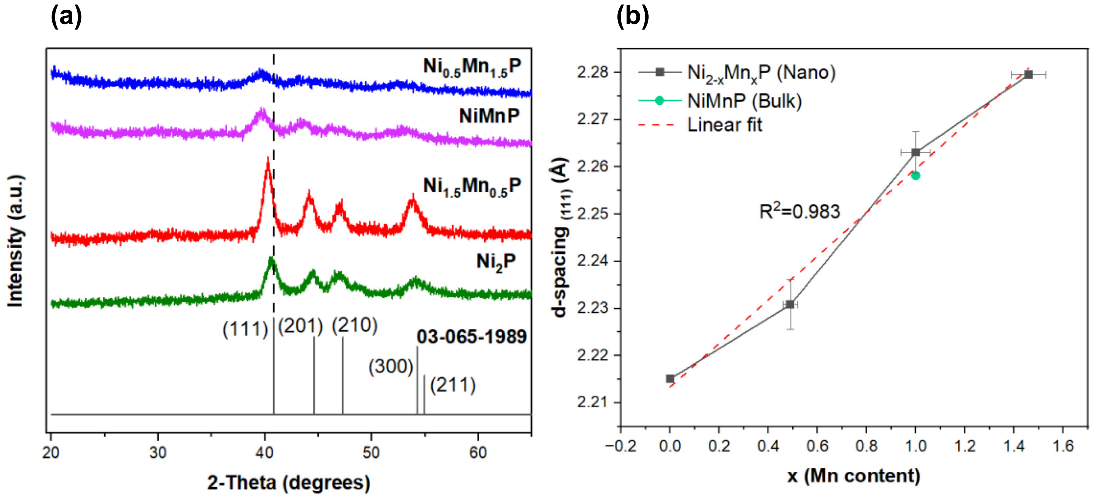

Figure 1. a) PXRD pattern for targeted compositions of $Ni_{2-x}Mn_xP$ nanoparticles (b) d-spacing for the (111) reflection vs. experimentally-determined Mn content from TEM/EDS. The green filled circle represents the reported value for bulk hexagonal NiMnP (PDF: 01-078-9553). The shoulder at 48.5° for Ni_2P is attributed to the presence of $Ni_{12}P_5$ as an impurity phase.

TEM data shows the particles to be spherical with low polydispersity (**Figure 2**) and the average particle sizes and standard deviations are shown in **Table 1** (histograms are shown in **Figure S11**). The general trend in TEM particle sizes follows that obtained for crystallite sizes from PXRD, suggesting the observation of increased broadening in the PXRD at high Mn concentrations is in fact reflective of decreasing size. However, for all compositions, sizes computed from TEM are consistently larger, which may reflect some crystalline disorder resulting in enhanced broadening in the diffraction pattern. A high-resolution TEM image of a particle of NiMnP (**Figure S12**) shows lattice fringes consistent with crystallinity and corresponding to a d-spacing of 2.269 Å that is close to the expected d-spacing for the (111) reflection of NiMnP[18] (2.258 Å) and the value obtained from PXRD (2.263 Å, **Figure 1a)**.

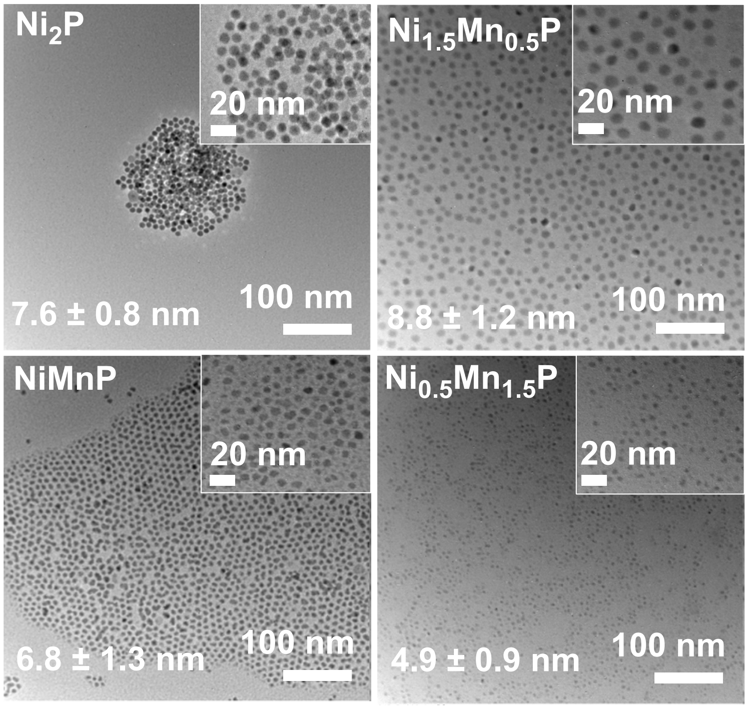

Figure 2. TEM images of $Ni_{2-x}Mn_xP$ nanoparticles. Particle diameters and standard deviations are obtained from histograms of ca. 200 particles (**Figure S11**).

Table 1. Scherrer crystallite and TEM sizes (nm) for $Ni_{2-x}Mn_xP$ (x≤1.5)

Targeted composition	**Actual composition**	**Scherrer crystallite size (nm)**				**TEM size (nm)**
		(111)	(201)	(210)	Average	
Ni_2P	$Ni_{2.00}P_{1.06}$	6.7	6.8	5.8	6.4	7.6 ± 0.8
$Ni_{1.5}Mn_{0.5}P$	$Ni_{1.51}Mn_{0.49}P_{1.21}$	9.9	7.4	6.8	7.9	8.8 ± 1.2
NiMnP	$Ni_{1.00}Mn_{1.00}P_{1.07}$	4.7	4.1	4.5	4.5	6.8 ± 1.3
$Ni_{0.5}Mn_{1.5}P$	$Ni_{0.54}Mn_{1.46}P_{0.97}$	3.5	3.3	3.1	3.3	4.9 ± 0.9

Histogram distributions for particle sizes of $Ni_{2-x}Mn_xP$ nanoparticles are shown in **Figure S11**.

Evaluation of geometry-normalized OER activity. To evaluate the OER activity, as-prepared nanoparticles of $Ni_{2-x}Mn_xP$ (x = 0.0, 0.5, 1.0, 1.5) were deposited onto carbon black and heated at 400 °C in a reducing environment to remove the ligands and then formulated into an ink. Aside from a decrease in intensity due to dilution of the nanoparticles, the PXRD pattern is unchanged after this processing (**Figure S13**), suggesting the structure and crystallite size are minimally impacted. The activity of the $Ni_{2-x}Mn_xP$ (x≤1.5) samples toward electrocatalytic OER at pH=14 was evaluated by cyclic voltammetry (CV) using a rotating disk electrode (RDE) and polarization curves are shown in **Figure 3a**. Current densities normalized by the geometric area of the glassy carbon working electrode are reported as mA/cm^2_{geo}. Except for the case of x=1.5, a quasi-reversible peak ascribed to oxidation of Ni^{2+} to Ni^{3+} is observed in the CV plots, and the peak position shifts as a function of Mn incorporation. Specifically, Ni_2P exhibits a broad peak from 1.31 V and stretching to 1.47 V with an onset potential at 1.21 V; incorporation of Mn (x=0.5) initially shifts the oxidation peak to higher voltage with an onset potential of 1.33 V, followed by a shift to lower voltage at x=1.0 (onset at 1.18 V) suggesting that the redox activity of the catalyst derived from NiMnP is more favorable for OER than that produced from Ni_2P and $Ni_{1.5}Mn_{0.5}P$. As noted above, there is no evidence of a discrete Ni oxidation peak in the x=1.5 sample. This "absence" is consistent with our prior work on $Ni_{2-x}Rh_xP$ nanoparticles;[19] as the Ni concentration in the nanoparticles decreases, the intensity of the Ni^{2+}/Ni^{3+} peak in the polarization curve decreases, disappearing into the background. Calculation of the overpotentials at 20 mA/cm^2 (**Figure 3b**) reveals a similar trend: x=0.5 exhibits a larger overpotential (445 mV) relative to Ni_2P (383.3 mV); and increasing the Mn incorporation to x=1.0 results in a decrease in overpotential to 322.5 mV, followed by a large increase at x =1.5 (530.0 mV). These results indicate that a 1:1 ratio of Ni:Mn in the precursor phosphide results in enhanced OER activity, with decreased or increased Mn concentrations resulting in decreased OER activity associated with a higher kinetic barrier. Calculated Tafel slope values from the CV diagrams **(Figure 3c)** are consistent with this analysis, with NiMnP exhibiting the smallest slope (185.6 mV/dec) relative to Ni_2P (417.5 mV/dec) and $Ni_{1.5}Mn_{0.5}P/Ni_{0.5}Mn_{1.5}P$ (~230-240 mV/dec).

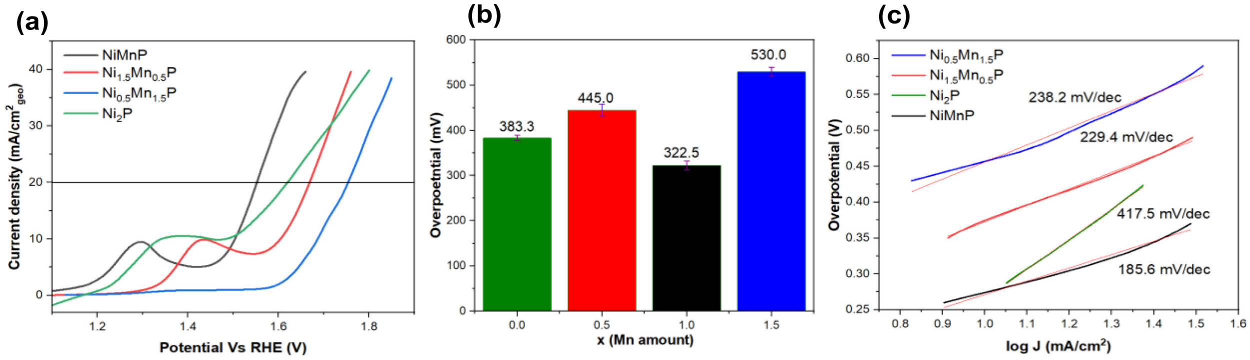

Figure 3. $Ni_{2-x}Mn_xP$, x=0, 0.5, 1, 1.5. (a) OER polarization curves, (b) bar graphs of the overpotential as a function of x, (c) Tafel plots/slopes.

Evaluation of electrochemical surface-area (ECSA) and morphological surface-area normalized OER activity. Geometry-normalized activity is dependent on the catalytic loading and does not consider the fact that the electrocatalytic reaction is a surface process.[20] Accordingly, we compared the geometry-normalized overpotential values in **Figure 3** with values determined from ECSA measurements (**Table S2, Figure S14, Figure 4**) and those calculated based on pre-catalyst particle size (**Table S2, Figure S15**).

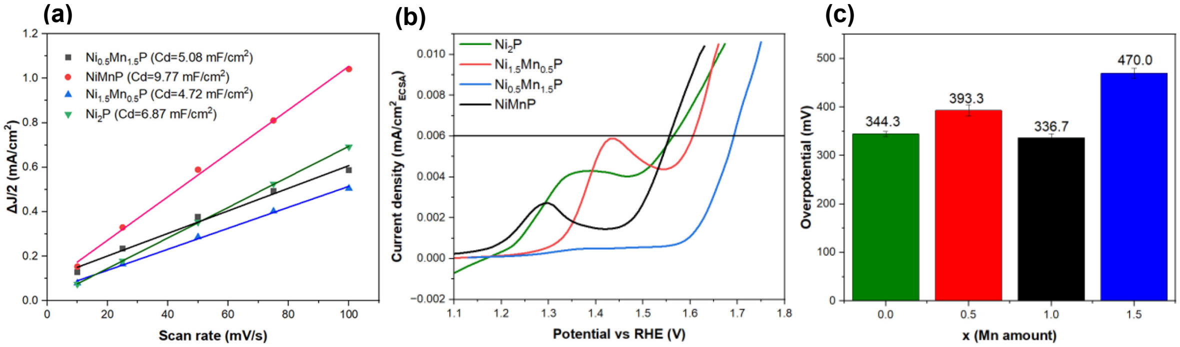

Figure 4. $Ni_{2-x}Mn_xP$ (x=0, 0.5, 1, 1.5): (a) current density vs scan rate plots for double layer capacitance calculation, (b) ECSA-normalized cyclic voltammograms, and (c) overpotentials obtained at 6 μA/cm$^2_{ECSA}$.

ECSA values were calculated from the double layer capacitance (C_d) computed by running cyclic voltammetry in the non-faradaic region at different scan rates for each composition. The calculated ECSA values do not reflect the absolute intrinsic activities of the catalysts, since the catalysts contain carbon black which contributes to the conductivity and capacity of the catalyst, and the true specific capacitance of the electrode is not known.[21] Therefore, we compare ECSA data on samples prepared identically, but with varying Mn content for comparison. CV diagrams in the acquired non-faradaic region (± 50 mV) at different scan rates for $Ni_{2-x}Mn_xP$ (x=0, 0.5, 1, 1.5) nanoparticles are shown in **Figure S14**. ΔJ (difference in cathodic and anodic current density) were plotted versus the scan rates and the slopes of these graphs give the C_d values for each compound **(Figure 4a)**. ECSA values are then calculated using the equation ECSA=C_d/C_s in which C_s is the specific capacitance in basic media, estimated to be 0.04 mF/cm² (**Table S2**), and the polarization curve current densities are normalized based on ECSA (**Figure 4b**). Comparing the overpotential of different compositions of $Ni_{2-x}Mn_xP$ at 6 μA/cm$^2_{ECSA}$ **(Figure 4c)** reveals the same trend found for geometric normalization, with NiMnP exhibiting the lowest overpotential compared to other compositions. Finally, the polarization curves were normalized based on the surface area calculated from the particle sizes obtained from TEM images and the number density of particles in the precatalyst film (**Table S2**). Once again, the same trend is observed as a function of Mn concentration (**Figure S15**). These data suggest that geometric current density is a reasonable proxy for establishing composition-dependent activity.

Stability of the NiMnP-derived catalyst to OER: The stability of the most active catalyst, derived from NiMnP, was probed in two ways: (1) by evaluating the current density as a function of potential by increasing the number of cycles; and (2) by assessing the current density at constant potential as a function of time. CV diagrams of NiMnP nanoparticles are shown for the first, the 200th and the 400th cycle, indicating the increase in the cycles leads to a decrease in current density and an increase in overpotential from 280.0 mV (first cycle) to 320.0 mV (200 cycles) and 390.0 mV (400 cycles) at 10 mA/cm^2_{geo} (**Figure 5a**). Furthermore, as the number of cycles increases, the intensity of the Ni^{2+} to Ni^{3+} oxidation peak is decreasing, suggesting that Ni^{3+} is not reverting to Ni^{2+} under our cycling conditions. A stability test done using controlled potential electrolysis (CPE) in 1.0 M KOH solution for 15 hours **(Figure 5b)** reveals an initial drop in current density over the first hour (a time-span corresponding roughly to 400 cycles), but the current density then exhibited no change during the rest of the experiment. In total, 80% of the current density is retained during the 15 hours of the stability test. Furthermore, Faradaic efficiency was calculated as 96.6% based on measuring O_2 generated in the head-space in reference to the total number of electrons passed during 1h of the CPE experiment. These data are consistent with the high selectivity of the NiMnP-derived catalyst towards the OER process (**Table S3, Figure S16**).

Composition and speciation changes for NiMnP pre- vs. post-OER. STEM elemental mapping for NiMnP (**Figure 6(a-d)**) and line scan mapping for a single as-prepared and unsupported NiMnP particle (**Figure 6(e,f)**) indicate homogeneous distribution of Ni, Mn, and P with near equal weighing within the particles and no evidence of phase-segregation. In contrast, after 15 h of CPE, HAADF and STEM elemental mapping images of the supported catalyst **(Figure 6g-j)** indicate that Ni and Mn remain co-localized in the particles, whereas the P signal is weak and poorly differentiated between background and particles, suggesting P loss. Line scan data **(Figure 6k-l)** are likewise consistent with a decrease in the P and Mn concentrations relative to Ni. To verify loss by dissolution, ICP-MS measurements were conducted on the supersaturated KOH solution after the 15 h stability test and revealed significant P dissolution is occurring, presumably as phosphate, accompanied by modest Mn dissolution (**Table S4**); no evidence of Ni was apparent. These results are consistent with the EDS chemical analysis collected on the catalyst before and after the 15 h CPE OER stability test (**Figures S17-18, Table S5)**, which reveals a ~ 69% loss of P and a ~2% loss of Mn.

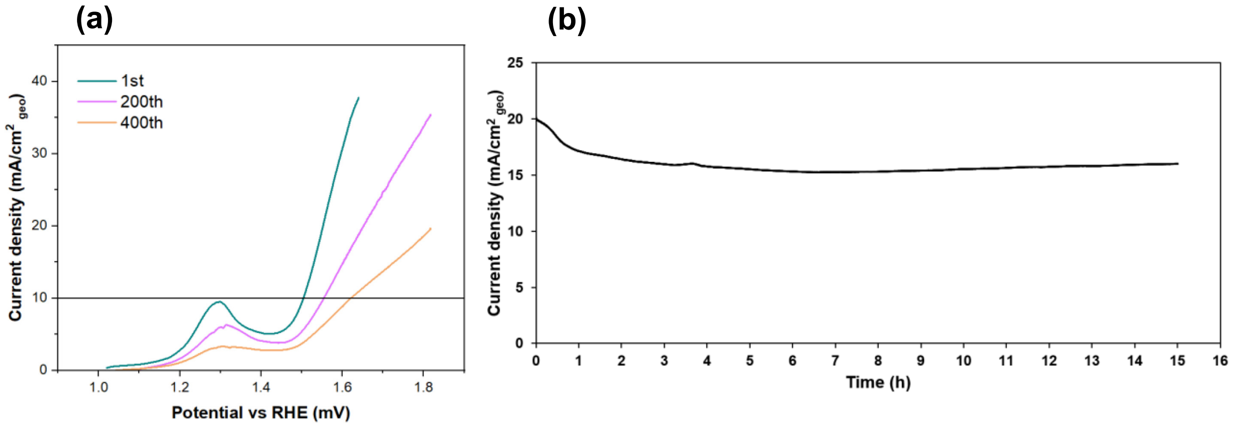

Figure 5. NiMnP (a) Current density vs. potential for different cycles, (b) stability test conducted by CPE over 15 hours carried out on a C-cloth substrate with a surface area of 1 cm^2 and applied potential of 2.1 V.

To probe surface speciation, XPS data were acquired for the supported pre-catalyst (a mixture of NiMnP supported on carbon black and annealed at 400°C), the pre-catalyst ink (ink solution before OER catalysis), and the post-catalysis ink (sample after 15 h CPE stability test). Peak fits of the high-resolution Ni2p, Mn2p, and P2p spectra were used to determine the relative amounts of the different chemical species (**Figures 7a-c**). Since the ink has Nafion,™ a fluorinated polymer, we were unable to use the Al K*α* source to collect Ni2p spectra on the pre-catalyst and post-catalysis inks, as there is strong overlap between the F KLL Auger and Ni2p peaks. Accordingly, Ni2p XPS data for those samples were obtained using a Mg K*α* source, with remaining spectra acquired using the conventional Al K*α* source **(Figure 7, Tables S6-S8)**.

In the supported pre-catalyst, the Ni2p$_{3/2}$ spectrum shows peaks at 853.7 eV, assigned to Ni-phosphide,[22] and 856.2 eV, which can be assigned either to Ni^{2+} or Ni^{3+} (differentiating between these two species is extremely challenging).[23,24] In contrast, the spectrum of

$Mn2p_{3/2}$ exhibits peaks at 641.4 eV and 642.8 eV, attributed to Mn^{3+} [25] and Mn^{4+}.[26] There is no evidence of a peak for Mn-phosphide (which should be close to the expected value for zerovalent Mn, 638.7 eV).[27] Finally, the $P2p_{3/2}$ spectrum has two peaks at 130.2 eV and 133.2 eV corresponding to metal phosphide[28] and metal phosphate[29] binding energies, respectively. Thus, both metals and phosphorus show clear evidence of surface oxidation due to air exposure, with the surface manganese being completely oxidized, consistent with the oxophilicity of reduced Mn.

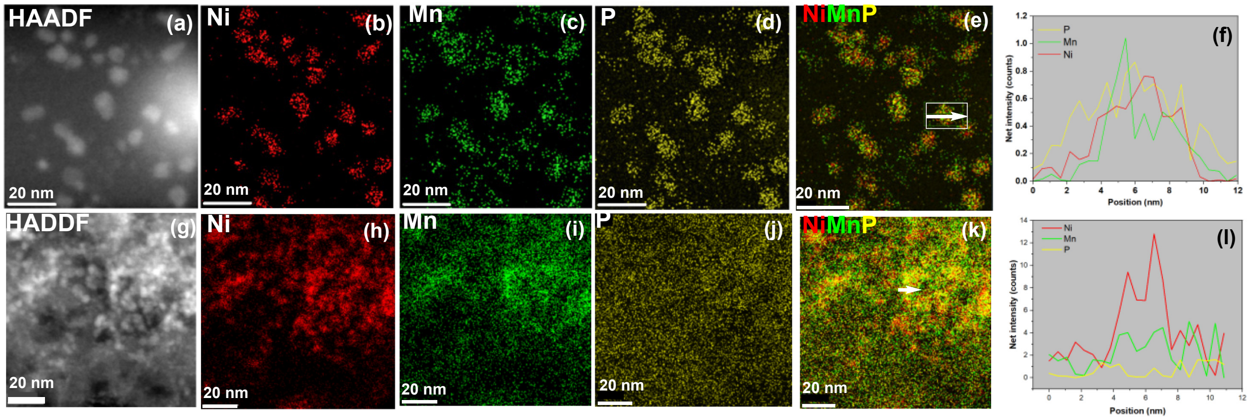

Figure 6. (a-f): HAADF, elemental mapping images for NiMnP nanoparticles, and line scan mapping for one NiMnP nanoparticle showing the co-localization of Ni, Mn, P. (g-l): HADDF, STEM elemental mapping, and line scan mapping for supported NiMnP nanoparticles after 15 h OER CPE stability test.

In the pre-catalyst ink with the Nafion,™ the $Ni2p_{3/2}$ spectrum (acquired with the Mg Kα source) has peaks at 853.1 eV for Ni-phosphide,[30, 31] 854.6 eV for Ni-O,[32] and a peak at 856.6 eV, which (again) can be assigned to Ni^{2+} or Ni^{3+}.[33,34] Compared to the supported pre-catalyst spectrum, the relative intensity of the Ni-phosphide peak relative to oxidized Ni has decreased, suggesting more oxidation occurs within the ink formulation. In addition, the spectrum for $Mn2p_{3/2}$ exhibits a peak at 643.0 eV for Mn^{4+},[26] which may be indicative of disproportionation of Mn^{3+} to Mn^{4+} and Mn^{2+} under neutral pH conditions (Mn^{3+} is only stable in the solid state, and under alkaline conditions).[35] However, we do not see clear evidence of Mn^{2+} in the spectrum of the pre-catalyst ink, although we cannot confidently rule out its presence, since the spectrum is noisy in the vicinity of where we would expect to see Mn^{2+} (~640 eV). Finally, the $P2p_{3/2}$ spectrum shows only peaks for metal-phosphate (133.9 eV), suggesting all the surface phosphide is also oxidized in the ink formulation.[36]

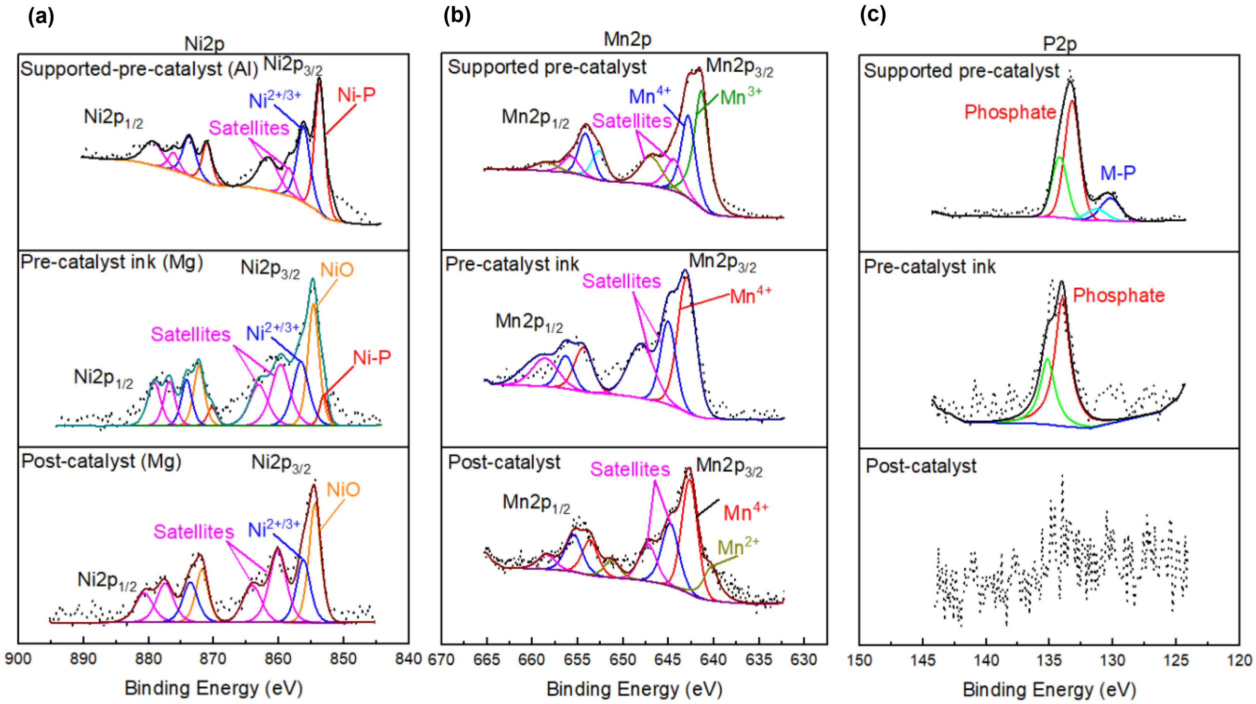

Figure 7. XPS spectra of Ni2p, Mn2p, and P2p for the supported pre-catalyst, pre-catalyst ink, and post-catalyst sample. Ni2p spectra of the inks were acquired with a Mg Kα source; all other spectra were acquired with an Al Kα source.

Post-catalysis, the Ni-phosphide peak completely disappears in the Ni2p$_{3/2}$ spectrum, leaving the two main peaks attributed to NiO (854.4 eV)[30] and Ni^{2+}/Ni^{3+} (856.2 eV).[33,24] For the Mn2p$_{3/2}$ spectrum, in addition to the peak associated with Mn^{4+} (642.7 eV) a peak at 640.3 eV is also observed that was not apparent pre-catalysis, attributed to Mn^{2+}.[37]. As previously indicated, Mn^{4+} and Mn^{2+} are expected upon disproportionation of Mn^{3+}, which is only stable at pH >9.[35] Since the post-catalysis specimen preparation for XPS involved rinsing with neutral water, the absence of Mn^{3+} in the XPS should not be conflated with an absence of Mn^{3+} under active catalytic conditions (pH = 14, applied potentials of ~1.4 V vs. RHE). Finally, there is virtually no detectible signal for P2p in the XPS. These data are consistent with accelerated oxidation upon OER testing and surface phosphate essentially dissolving in solution. These data suggest that NiMnP is a precatalyst that undergoes oxidation during the OER process to produce the catalyst, likely a bimetallic oxide/hydroxide.

Comparison of catalytic activity: NiMnP and CoMnP. To better frame the activity of the NiMnP pre-catalyst within the context of other bimetallic Mn phosphides, we sought to compare to CoMnP. It was shown in previous work that the CoMnP-derived catalyst has the highest OER activity among different compositions in $Co_{2-x}Mn_xP$ ($x \leq 1.4$), with an overpotential of 330.0 mV at 10 mA/cm^2_{geo}. However, the reported sample was not processed in the same way as the NiMnP particles produced here (there was no thermal annealing of the supported catalyst to eliminate ligands). For an apples-to-apples comparison, we synthesized CoMnP nanoparticles with some modifications from the previous work (**Figure S19-20**) and then the sample was supported on carbon, annealed, and the ink prepared, all in the same way as for NiMnP. OER catalytic testing (**Figure 8**) suggest that the CoMnP-derived catalyst requires an overpotential of 302.5 mV to achieve a geometric current density of 10 mA/cm^2_{geo}, representing a drop of ~28 mV vs. the previously reported sample without thermal annealing, but still significantly higher than NiMnP (280.0 mV). We attribute the reduced overpotential upon thermal annealing to elimination of surface ligands that block active sites.[7] Corresponding values at 20 mA/cm^2_{geo} are 355.0 mV (CoMnP) and 322.5 mV (NiMnP).

The same trend was observed for surface-area-normalized data computed based on ECSA (from double-layer capacitance calculations) or particle size/number density (from TEM size data and weight loading) as shown in **Figure S21** and **Figure S22**. While we did not explicitly compare the most Mn-rich $Fe_{2-x}Mn_xP$ phase that we could synthetically access ($Fe_{1.1}Mn_{0.9}P$), we can confidently say that the $Fe_{2-x}Mn_xP$ system is the least active of the three, since the original report of $Fe_{1.1}Mn_{0.9}P$ with thermal annealing to remove ligands shows the minimum overpotential of 350.0 mV at 10 mA/cm^2_{geo}.

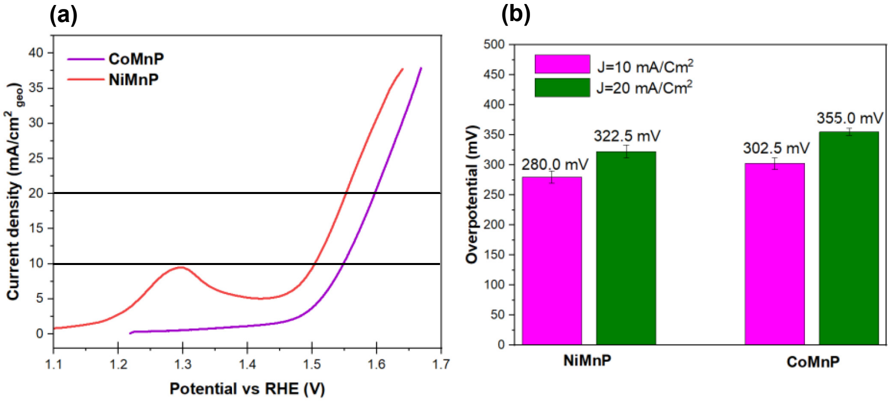

Figure 8. (a) Polarization curves and (b) overpotentials at 10 and 20 mA/cm^2 for NiMnP and CoMnP.

DISCUSSION

Phase stability of $M_{2-x}Mn_xP$ (M=Fe, Co, Ni). Despite many attempts, we have not been able to produce Mn_2P by colloidal routes, although this is a known thermodynamic phase. Instead, MnP forms with Mn_xO_y as a byproduct.[6] Indeed, the discovery of $Co_{2-x}Mn_xP$ arose from unsuccessful attempts to prepare $Co_{1-x}Mn_xP$, i.e., to substitute Co into MnP.[6] The relatively facile incorporation of Mn into Co_2P enabled compositions with $x \leq 1.4$ to be prepared and tested for electrocatalytic OER. In contrast, incorporation of Mn into Fe_2P proved to be a significant challenge, requiring a large excess of Mn precursor and multiple additions to achieve x up to 0.9. The synthesis of $Ni_{2-x}Mn_xP$ proceeded differently from $Co_{2-x}Mn_xP$ and $Fe_{2-x}Mn_xP$, where zerovalent carbonyl precursors of Co (or Fe) and Mn were introduced at the same time. Instead, a Ni(II) salt was employed and reduced *in situ* with oleylamine, a mild reductant, to produce amorphous Ni-P particles, and then $Mn_2(CO)_{10}$ was injected in a second step. The pre-reduction of Ni is crucial for the reaction success, in order to prevent oxidation of Mn(0) by Ni(II). In principle, any Ni(II) salt should work; however, we employed $Ni(acac)_2$ as this precursor was available to us in anhydrous form. Likewise, Mn(II,III) salts are very challenging to reduce (requiring n-butyl Li[38]), motivating the selection of $Mn_2(CO)_{10}$. With small modifications of reaction conditions (and the use of excess Mn equivalents), it was possible to incorporate Mn into 75% of the metal sites ($Ni_{0.5}Mn_{1.5}P$), which represents the maximum uptake of all systems studied to date.

Intriguingly, while $M_{2-x}Mn_xP$ (M = Fe, Co, Ni) phases can crystallize as hexagonal or orthorhombic, the structures are very similar, with two distinct metal sites: square pyramidal (M_1) and tetrahedral (M_2), as illustrated for the hexagonal phase in **Figure 9**. Given the breadth of the PXRD peaks (due to the small sizes of the nanoparticles) it is not possible to distinguish between hexagonal and orthorhombic structures.[18,39-42] In the thermodynamic bulk structure, site positioning is driven by atomic radius, with the larger metal (Mn, 137 pm) preferentially occupying the M_1 site and the smaller metal (Fe, Co, Ni; 125-126 pm), the M_2 site. However, given the relatively low temperature at which nanoparticles are synthesized, it is possible that positional disorder occurs. Nevertheless, in the case of $Ni_{2-x}Mn_xP$, it is clear that incorporation of Mn is not producing tensile strain, as previously suggested for samples prepared solvothermally,[13] as the diffraction peaks follow Vegard's law. Another universal effect of Mn incorporation in Ni_2P, Co_2P, and Fe_2P is a general decrease in the particle sizes.[6, 7] While the origin of this effect is unclear, a decrease might be expected to produce enhanced activity for similar weight loadings. However, this effect would appear to be modest, as normalization of current density to ECSA or surface area computed based on particle size gives the same trends as the geometrically normalized data.

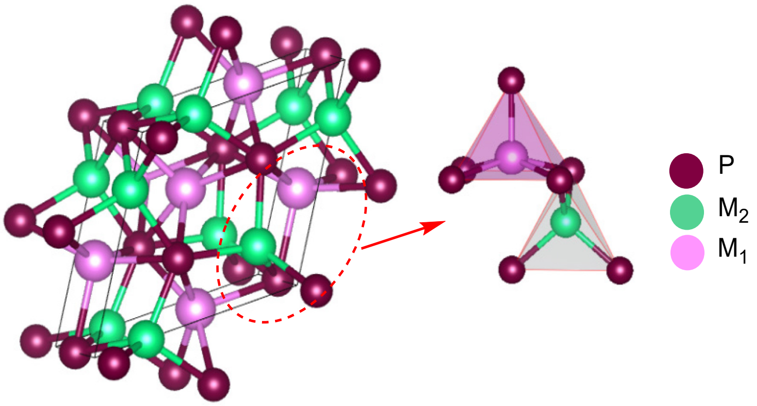

Figure 9. Crystal structure of hexagonal M_2P showing the two types of M sites, M_1 (square pyramidal) and M_2 (tetrahedral).

Compositionally modulated OER activity. Compositionally-dependent activities for $M_{2-x}Mn_xP$ (M = Fe, Co, Ni) are observed in which the maximum activity is obtained at or near the 1:1 M:Mn ratio.[6, 7, 43] For Fe, the highest Mn loading that we could achieve is $x = 0.9$ but we note a consistent drop in overpotential as $x = 1$ is approached. For M = Co and Ni, where the Mn solubility is greater, evidence of a "sweet spot" at the 1:1 ratio is very clear, with increasing Mn incorporation beyond this requiring a larger overpotential for OER. It is tempting to attribute this optimal activity to a cooperative effect due to proximity of the two different metals on adjacent sites (since tetrahedral and square pyramidal sites share an edge), but the phosphide is clearly not the catalyst for OER. However, intimate 1:1 mixing in the pre-catalyst may enable a similar mixing in the active (oxidized) catalyst that forms on the surface of $M_{2-x}Mn_xP$ (M = Fe, Co, Ni) under active catalytic conditions.[44] In the specific case of NiMnP, the increase in OER activity of the NiMnP-derived catalyst relative to that produced from Ni_2P can be postulated to arise from one of two scenarios: (1) One metal site is active for OER and the second metal serves to modify the electronic structure resulting in enhanced activity (2) Both Ni and Mn sites are catalytically active, operating in an additive manner (both sites independently active), or cooperatively in a synergistic manner. Based on the data, and current understanding from the OER literature of oxides and hydroxides, we think the actual case is a combination of these two scenarios, as described below.

A number of papers have described increased OER activity (decreased overpotential) upon Mn-incorporation into Ni hydroxides and upon Ni-incorporation into Mn oxides. Very recently, Yin et al.,[45] evaluated the OER performance of Mn-doped $Ni(OH)_2$ nanosheets and hypothesized that Mn incorporation modifies the redox potential of the $Ni^{2+/3+}$ couple to lead to enhanced activity of that site, and that the Mn site is also active. Specifically, incorporation of 26% by mole Mn into the β-$Ni(OH)_2$ precatalyst results in a structure change to the α-phase (α-$Ni_{0.74}Mn_{0.26}(OH)_2$) and a shift in the $Ni^{2+/3+}$ oxidation wave from 1.4 V for β-$Ni(OH)_2$ to 1.35 V for α-$Ni_{0.74}Mn_{0.26}(OH)_2$ vs. NHE. This shift reflects the activation of Ni by Mn, which is indicative of charge transfer, similar to that observed by Goodenough and co-workers[46] from Ni^{2+} to Mn^{4+} in $LaNi_{1-x}Mn_xO_3$ ($0 \leq x \leq 0.2$ and $x=0.5$), mediated by bridging oxo groups. Such shifts in $Ni^{2+/3+}$ redox potential are also seen when Ni is incorporated into manganese oxide catalysts, where it is also associated with a decreased overpotential for alkaline OER.[47] With respect to evidence of Mn site activity in α-$Ni_{0.74}Mn_{0.26}(OH)_2$, *in situ* Raman spectroscopic data support formation of both MnOOH and γ-NiOOH above potentials of 1.3 and 1.4 V, respectively, both of which are purported active phases for alkaline OER electrocatalysis.

In keeping with the hypothesis that the catalyst is produced *in situ* by oxidation of the NiMnP precatalyst in alkaline media at positive potentials, XPS data (**Figure 7c**) reveals that the surface phosphide is converted to phosphate, which is solubilized in the basic media, exposing the metal ions to hydroxide solution. Likewise, surface nickel phosphide (Ni^0) present in the supported pre-catalyst and pre-catalyst ink, is completely oxidized after OER, producing $Ni^{2+/3+}$ (note: it is challenging to distinguish between Ni^{2+} and Ni^{3+} by XPS, **Figure 7a**). In the case of Mn2p spectra **(Figure 7b)** we see no evidence of surface manganese phosphide in the supported pre-catalyst, consistent with the oxophilicity of Mn. Rather, a combination of Mn^{3+} and Mn^{4+} is observed. However, when the supported pre-catalyst is dispersed into the neutral Nafion/water/alcoholic solution to prepare the ink, only Mn^{4+} is observed. As described previously, the disappearance of Mn^{3+} is in keeping with known redox stability of manganese oxides/hydroxides, in which Mn^{3+} is not stable at pH < 9 due to the disproportionation reaction, converting to Mn^{2+} and Mn^{4+}.[35] Post-catalysis, in samples rinsed with neutral water, both Mn^{4+} and Mn^{2+} are evident, as would be expected from disproportionation of Mn^{3+}.[35]

The hypothesis that activation of the Ni site is induced by Mn is supported by polarization curves that show a shifting in the Ni^{2+}/Ni^{3+} oxidation peak in the CV diagram from 1.31 V (Ni_2P) to 1.18 V (NiMnP) consistent with a reduction in the $Ni^{2+/3+}$ redox potential, and more facile formation of catalytically active Ni^{3+}. We presume this is due to charge transfer from Ni^{2+} to Mn^{4+}, as previously discussed. This charge transfer can increase the partial charge on the Ni site and decrease the partial charge on Mn site creating $Ni^{+2+\delta}$-O-$Mn^{+4-\delta}$ and facilitating the formation, upon application of a suitable potential, of Ni^{3+} and Mn^{3+} active sites for catalysis.[35] The formation of Mn^{3+} at high pH and at positive potentials of ~1.4 V occurs by conproportionation, in which Mn^{2+} and Mn^{4+} produce Mn^{3+} ($Mn^{4+} + Mn^{2+} \rightarrow 2\ Mn^{3+}$), which is the active species in the OER process.[35] Formation of Mn^{3+} is only indirectly captured by the XPS data, which shows Mn^{4+} and Mn^{2+} post-catalysis, consistent with disproportionation upon neutralization and drying of the sample.

The role of Mn in activating Ni is also indirectly supported by the observation that shifting of the Ni^{2+}/Ni^{3+} oxidation peak to higher potential over time, and decreasing of the peak intensity (**Figure 5a**), is correlated with leaching of Mn into the solution and partial deactivation of the catalyst (decrease in current density, **Figure 5b**). During dissolution, Mn active sites are lost, and Ni sites are rendered less active because of their loss. In the absence of Mn, i.e., with Ni_2P as a pre-catalyst, no $Ni^{2+/3+}$ redox peak shift is observed, even after many OER cycles.[48] In this context, we see charge transfer as a critical element in augmenting activity of bimetallic OER catalysts relative to monometallic systems.

Finally, in the context of understanding the relative activity of $M_{2-x}Mn_xP$ (M = Fe, Co, Ni) precatalysts for OER in base, and considering charge transfer, the observed trend: $Fe_{1.1}Mn_{0.9}P$ < CoMnP < NiMnP, is consistent with an increase in charge transfer when more electropositive Mn (χ=1.55) is combined with increasingly more electronegative metals. That is, the activity correlates with an increase in the electronegativity difference between Mn and Fe ($\Delta\chi$=0.28) vs. Co ($\Delta\chi$=0.33) vs. Ni ($\Delta\chi$=0.36). Moreover, as the extent of charge transfer also depends on the relative ratio of Mn:M (M = Fe, Co, Ni);[46] the fact that activity appears to be optimized at a 1:1 ratio, regardless of electronegativity difference (identity of M), suggests that the Mn and M sites may in fact be acting synergistically, and not merely in an additive fashion.

CONCLUSIONS

$Ni_{2-x}Mn_xP$ nanoparticles have been synthesized as discrete nanoparticles of diameter 5-10 nm, depending on composition, and with low-polydispersity (< 20% standard deviation) achieving up to 75% Mn incorporation ($x \leq 1.5$). Moreover, a new method was developed that successfully removed nanoparticles of Mn_xO_y produced as a byproduct in the synthesis of samples with $x \geq 1$ by phase-transfer of Mn_xO_y into an aqueous oleic acid solution. Notably, the $Ni_{2-x}Mn_xP$ system is capable of greater Mn incorporation when compared to $Co_{2-x}Mn_xP$ ($x \leq 1.4$) and $Fe_{2-x}Mn_xP$ ($x \leq 0.9$). OER evaluation of the $Ni_{2-x}Mn_xP$ nanoparticles (x = 0, 0.5, 1.0, 1.5) reveal the most active phase to be that derived from the NiMnP (x = 1.0) precatalyst, with an overpotential of 280 mV at 10 mA/cm^2_{geo}. XPS and chemical analysis are consistent with transformation of NiMnP to oxide/hydroxide under active OER conditions, and with phosphorus oxidized to phosphate, which is solubilized in the electrolyte. Despite the initial (over 1 h) decrease in activity (attributed in part to some dissolution of Mn), 80% of the current density is retained during a 15 h stability test. The activity of the *in situ* prepared oxide/hydroxide catalyst is attributed to (1) charge transfer from Mn to Ni mediated by bridging oxo groups, decreasing the redox potential for the $Ni^{2+/3+}$ couple and favoring formation of Ni^{3+}, and (2) the stabilization of Mn^{3+} as an active co-catalyst. Moreover, NiMnP outperforms CoMnP (η=302.5 mV at 10 mA/cm^2_{geo}) and $Fe_{1.1}Mn_{0.9}P$ (η=350.0 mV at 10 mA/cm^2_{geo}), which we hypothesize reflects differing extents of charge transfer, as governed by the electronegativity difference between Mn and Fe vs. Co vs. Ni. The presence of a “sweet-spot” at or near the 1:1 Mn:M (M = Fe, Co, Ni) ratio suggests the possibility of synergistic activity between Mn and the secondary metal, M.

Supporting Information: Scheme for the synthesis of $Ni_{0.5}Mn_{1.5}P$ nanoparticles. Figures of representative EDS spectra, PXRD and TEM data for $Ni_{2-x}Mn_xP$ ($x \leq 1.5$) as a function of synthetic conditions and of CoMnP; Particle size histograms for $Ni_{2-x}Mn_xP$ samples used in OES testing; High resolution TEM image of a NiMnP nanoparticle; CV diagrams for ECSA calculations of $Ni_{2-x}Mn_xP$ and CoMnP; Polarization curves normalized based on ECSA (CoMnP) and surface area (CoMnP, NiMnP); Faradaic efficiency plot for NiMnP. Tables of average EDS composition for $Ni_{2-x}Mn_xP$ samples; ECSA and surface area calculations for $Ni_{2-x}Mn_xP$ and CoMnP; data for faradaic efficiency plot; ICP-MS data on electrolyte solution before and after catalytic testing with NiMnP; XPS reference data for Ni, Mn, and P.

Corresponding Author: Stephanie L. Brock − Department of Chemistry, Wayne State University, Detroit 48202 Michigan, United States; orcid.org/0000-0002-0439-302X; Email: sbrock@chem.wayne.edu

Author Contributions: FA conducted the experimental investigation, analyzed and validated the data, wrote the original manuscript draft, and reviewed and edited the manuscript. SSP conducted analysis and validation of XPS data and reviewed and edited the manuscript. SLB conceived of the project, acquired the funding, supervised the research and reviewed and edited the manuscript. All authors have given approval to the final version of the manuscript.

ACKNOWLEDGMENTS: We thank the National Science Foundation (NSF) for support (DMR-1904775). This work used PXRD, TEM, UPS/XPS and ICP-MS from the Lumigen Instrument Center, Department of Chemistry, Wayne State University, purchased with assistance from NSF grant numbers 1427926, 2018587, and 1849578. Furthermore, the authors acknowledge the Texas A&M University Materials Characterization Core Facility (RRID:SCR_022202) for collecting Mg Kα source data using a dual-source Al/Mg XPS.

References:

(1) Suen, N.-T.; Hung, S.-F.; Quan, Q.; Zhang, N.; Xu, Y.-J.; Chen, H. M. Electrocatalysis for the oxygen evolution reaction: recent development and future perspectives. *Chem. Soc. Rev.* **2017**, *46* (2), 337-365.

(2) McCrory, C. C. L.; Jung, S.; Peters, J. C.; Jaramillo, T. F. Benchmarking Heterogeneous Electrocatalysts for the Oxygen Evolution Reaction. *J. Am. Chem. Soc.* **2013**, *135* (45), 16977-16987.

(3) Trasatti, S. Electrocatalysis by oxides - Attempt at a unifying approach. *J. Electroanal. Chem. Interf. Electrochem.* **1980**, *111* (1), 125-131.

(4) Popczun, E. J.; McKone, J. R.; Read, C. G.; Biacchi, A. J.; Wiltrout, A. M.; Lewis, N. S.; Schaak, R. E. Nanostructured Nickel Phosphide as an Electrocatalyst for the Hydrogen Evolution Reaction. *J. Am. Chem. Soc.* **2013**, *135* (25), 9267-9270.

(5) Layan Savithra, G. H.; Muthuswamy, E.; Bowker, R. H.; Carrillo, B. A.; Bussell, M. E.; Brock, S. L. Rational Design of Nickel Phosphide Hydrodesulfurization Catalysts: Controlling Particle Size and Preventing Sintering. *Chem. Mater.* **2013**, *25* (6), 825-833.

(6) Li, D.; Baydoun, H.; Verani, C. N.; Brock, S. L. Efficient Water Oxidation Using CoMnP Nanoparticles. *J. Am. Chem. Soc.* **2016**, *138* (12), 4006-4009.

(7) Li, D.; Baydoun, H.; Kulikowski, B.; Brock, S. L. Boosting the Catalytic Performance of Iron Phosphide Nanorods for the Oxygen Evolution Reaction by Incorporation of Manganese. *Chem. Mater.* **2017**, *29* (7), 3048-3054.

(8) Li, W.; Xiong, D.; Gao, X.; Liu, L. The oxygen evolution reaction enabled by transition metal phosphide and chalcogenide pre-catalysts with dynamic changes. *Chem Comm.* **2019**, *55* (60), 8744-8763.

(9) Nguyen, D. C.; Tran, D. T.; Luyen Doan, T. L.; Kim, N. H.; Lee, J. H. Constructing MoPx@MnP$_y$ Heteronanoparticle-Supported Mesoporous N,P-Codoped Graphene for Boosting Oxygen Reduction and Oxygen Evolution Reaction. *Chem. Mater.* **2019**, *31* (8), 2892-2904.

(10) Downes, C. A.; Van Allsburg, K. M.; Tacey, S. A.; Unocic, K. A.; Baddour, F. G.; Ruddy, D. A.; LiBretto, N. J.; O'Connor, M. M.; Farberow, C. A.; Schaidle, J. A.; et al. Controlled Synthesis of Transition Metal Phosphide Nanoparticles to Establish Composition-Dependent Trends in Electrocatalytic Activity. *Chem. Mater.* **2022**, *34* (14), 6255-6267

(11) Xu, J.; Li, J.; Xiong, D.; Zhang, B.; Liu, Y.; Wu, K.-H.; Amorim, I.; Li, W.; Liu, L. Trends in activity for the oxygen evolution reaction on transition metal (M = Fe, Co, Ni) phosphide pre-catalysts. *Chem. Sci.* **2018**, *9* (14), 3470-3476.

(12) Man, H.-W.; Tsang, C.-S.; Li, M. M.-J.; Mo, J.; Huang, B.; Lee, L. Y. S.; Leung, Y.-c.; Wong, K.-Y.; Tsang, S. C. E. Tailored transition metal-doped nickel phosphide nanoparticles for the electrochemical oxygen evolution reaction (OER). *Chem Comm.* **2018**, *54* (62), 8630-8633.

(13) Sarkar, S.; Dheer, L.; Vinod, C. P.; Thapa, R.; Waghmare, U. V.; Peter, S. C. Stress-Induced Electronic Structure Modulation of Manganese-Incorporated Ni_2P Leading to Enhanced Activity for Water Splitting. *ACS Appl. Energy Mater.* **2020**, *3* (2), 1271-1278.

(14) Muthuswamy, E.; Savithra, G. H. L.; Brock, S. L. Synthetic Levers Enabling Independent Control of Phase, Size, and Morphology in Nickel Phosphide Nanoparticles. *ACS Nano* **2011**, *5* (3), 2402-2411.

(15) Holder, C. F.; Schaak, R. E. Tutorial on Powder X-ray Diffraction for Characterizing Nanoscale Materials. *ACS Nano* **2019**, *13* (7), 7359-7365.

(16) Bondarchuk, O.; LaGrow, A. P.; Kvasha, A.; Thieu, T.; Ayerbe, E.; Urdampilleta, I. On the X-ray photoelectron spectroscopy analysis of $LiNi_xMn_yCo_zO_2$ material and electrodes. *Appl. Surf. Sci.* **2021**, *535*, 147699.

(17) Zhang, Y.; Gao, L.; Hensen, E. J. M.; Hofmann, J. P. Evaluating the Stability of Co_2P Electrocatalysts in the Hydrogen Evolution Reaction for Both Acidic and Alkaline Electrolytes. *ACS Energy Lett.* **2018**, *3* (6), 1360-1365.

(18) A. Roger, J. P. S., and R. Fruchart. Les proprietes cristallographiques et magnetiques des solutions solides entre les phosphures Ni_2P-Co_2P-Fe_2P-Mn_2P et Cr_2P. *Annales de Chimie* **1969**, *4*, 79-91.

(19) Batugedara, T. N.; Brock, S. L. Role of Noble- and Base-Metal Speciation and Surface Segregation in $Ni_{2-x}Rh_xP$ Nanocrystals on Electrocatalytic Water Splitting Reactions in Alkaline Media. *Chem. Mater.* **2022**, *34* (10), 4414-4427.

(20) Wei, C.; Sun, S.; Mandler, D.; Wang, X.; Qiao, S. Z.; Xu, Z. J. Approaches for measuring the surface areas of metal oxide electrocatalysts for determining their intrinsic electrocatalytic activity. *Chem Soc Rev.* **2019**, *48* (9), 2518-2534.

(21) Fabbri, E.; Mohamed, R.; Levecque, P.; Conrad, O.; Kötz, R.; Schmidt, T. J. Composite Electrode Boosts the Activity of $Ba_{0.5}Sr_{0.5}Co_{0.8}Fe_{0.2}O_{3-\delta}$ Perovskite and Carbon toward Oxygen Reduction in Alkaline Media. *ACS Catal.* **2014**, *4* (4), 1061-1070.

(22) Liu, Y.; Ding, M.; Deng, X.; Zhang, Y.; Zhao, G. Bimetal phosphide as high efficiency and stable bifunctional electrocatalysts for hydrogen and oxygen evolution reaction in alkaline solution. *RSC Adv* **2022**, *12* (15), 9051-9057.

(23) Liu, H.; Zhao, Q.; Wang, K.; Lu, Z.; Feng, F.; Guo, Y. Facile synthesis of polypyrrole nanofiber (PPyNF)/NiO_x composites by a microwave method and application in supercapacitors. *RSC Adv.* **2019**, *9* (12), 6890-6897.

(24) Wang, Y.; Tao, S.; Lin, H.; Han, S.; Zhong, W.; Xie, Y.; Hu, J.; Yang, S. NaBH4 induces a high ratio of Ni^{3+}/Ni^{2+} boosting OER activity of the NiFe LDH electrocatalyst. *RSC Adv.* **2020**, *10* (55), 33475-33482.

(25) Yang, S.; Guo, Y.; Yan, N.; Wu, D.; He, H.; Xie, J.; Qu, Z.; Jia, J. Remarkable effect of the incorporation of titanium on the catalytic activity and SO2 poisoning resistance of magnetic Mn–Fe spinel for elemental mercury capture. *Appl. Catal., B.* **2011**, *101* (3), 698-708.

(26) Stranick, M. A. MnO_2 by XPS. *Surface Science Spectra* **1999**, *6* (1), 31-38.

(27) Blanchard, P. E. R.; Grosvenor, A. P.; Cavell, R. G.; Mar, A. X-ray Photoelectron and Absorption Spectroscopy of Metal-Rich Phosphides M_2P and M_3P (M = Cr−Ni). *Chem. Mater.* **2008**, *20* (22), 7081-7088.

(28) Lv, X.; Ren, J.; Wang, Y.; Liu, Y.; Yuan, Z.-Y. Well-Defined Phase-Controlled Cobalt Phosphide Nanoparticles Encapsulated in Nitrogen-Doped Graphitized Carbon Shell with Enhanced Electrocatalytic Activity for Hydrogen Evolution Reaction at All-pH. *ACS Sustain. Chem. Eng.* **2019**, *7* (9), 8993-9001.

(29) Rho, Y.-H.; Nazar, L. F.; Perry, L.; Ryan, D. Surface Chemistry of $LiFePO_4$ Studied by Mössbauer and X-Ray Photoelectron Spectroscopy and Its Effect on Electrochemical Properties. *J. Electrochem. Soc.* **2007**, *154* (4), A283.

(30) Lu, X.; Baker, M. A.; Anjum, D. H.; Papawassiliou, W.; Pell, A. J.; Fardis, M.; Papavassiliou, G.; Hinder, S. J.; Gaber, S. A. A.; Gaber, D. A. A.; et al. Nickel Phosphide Nanoparticles for Selective Hydrogenation of SO_2 to H_2S. *ACS Appl. Nano Mater.* **2021**, *4* (7), 6568-6582.
(31) Han, A.; Chen, H.; Sun, Z.; Xu, J.; Du, P. High catalytic activity for water oxidation based on nanostructured nickel phosphide precursors. *Chem Comm.* **2015**, *51* (58), 11626-11629.
(32) Peck, M. A.; Langell, M. A. Comparison of Nanoscaled and Bulk NiO Structural and Environmental Characteristics by XRD, XAFS, and XPS. *Chem. Mater.* **2012**, *24* (23), 4483-4490.
(33) Fa, D.; Yu, B.; Miao, Y. Synthesis of ultra-long nanowires of nickel phosphate by a template-free hydrothermal method for electrocatalytic oxidation of glucose. *Colloids Surf. A Physicochem. Eng. Asp.* **2019**, *564*, 31-38.
(34) Xiong, D.; Li, W.; Liu, L. Vertically Aligned Porous Nickel(II) Hydroxide Nanosheets Supported on Carbon Paper with Long-Term Oxygen Evolution Performance. *Chem. Asian J.* **2017**, *12* (5), 543-551.
(35) Takashima, T.; Hashimoto, K.; Nakamura, R. Mechanisms of pH-Dependent Activity for Water Oxidation to Molecular Oxygen by MnO_2 Electrocatalysts. *J. Am. Chem. Soc.* **2012**, *134* (3), 1519-1527.
(36) Cecilia, J. A.; Infantes-Molina, A.; Rodríguez-Castellón, E.; Jiménez-López, A. A novel method for preparing an active nickel phosphide catalyst for HDS of dibenzothiophene. *J. Catal.* **2009**, *263* (1), 4-15.
(37) Drouet, C.; Laberty, C.; Fierro, J. L. G.; Alphonse, P.; Rousset, A. X-ray photoelectron spectroscopic study of non-stoichiometric nickel and nickel–copper spinel manganites. *Int. J. Inorg. Mater.* **2000**, *2* (5), 419-426.
(38) Bondi, J. F.; Oyler, K. D.; Ke, X.; Schiffer, P.; Schaak, R. E. Chemical Synthesis of Air-Stable Manganese Nanoparticles. *J. Am. Chem. Soc.* **2009**, *131* (26), 9144-9145.
(39) Fruchart, R.; Roger, A.; Senateur, J. Crystallographic and magnetic properties of solid solutions of the phosphides M_2P, M= Cr, Mn, Fe, Co, and Ni. *J. Appl. Phys.* **1969**, *40* (3), 1250-1257.
(40) Radhakrishna, P.; Fujii, H.; Brown, P.; Doniach, S.; Reichardt, W.; Schweiss, P. Magnetic and neutron diffraction studies on $(Co_{1-x}Mn_x)_2P$. *J. Condens. Matter Phys.* **1990**, *2* (14), 3359.
(41) Srivastava, B.; Ericsson, T.; Haggstrom, L.; Verma, H.; Andersson, Y.; Rundqvist, S. A Mossbauer study of the $(Fe_{1-x}Mn_x)_2P$ system. *J. Phys. C: Solid State Phys.* **1987**, *20* (3), 463.
(42) Średniawa, B.; Zach, R.; Chajec, W.; Duraj, R.; Tobola, J.; Nizioł, S.; Kaprzyk, S.; Fruchart, D.; Bacmann, M. Magnetism and electronic structure of the $(Co_{1-x}Mn_x)_2P$ system. *J. Magn. Magn. Mater.* **2002**, *242-245*, 931-934.
(43) Zhang, Y.; Li, N.; Zhang, Z.; Li, S.; Cui, M.; Ma, L.; Zhou, H.; Su, D.; Zhang, S. Programmable Synthesis of Multimetallic Phosphide Nanorods Mediated by Core/Shell Structure Formation and Conversion. *J. Am. Chem. Soc.* **2020**, *142* (18), 8490-8497.

(44) Ding, H.; Liu, H.; Chu, W.; Wu, C.; Xie, Y. Structural Transformation of Heterogeneous Materials for Electrocatalytic Oxygen Evolution Reaction. *Chem. Rev.* **2021**, *121* (21), 13174-13212.

(45) Yin, T.-T.; Xu, H.-M.; Zhang, X.-L.; Su, X.; Shi, L.; Gu, C.; Han, S.-K. Mn-Incorporation-Induced Phase Transition in Bottom-Up Synthesized Colloidal Sub-1-nm $Ni(OH)_2$ Nanosheets for Enhanced Oxygen Evolution Catalysis. *Nano Lett.* **2023**, *23* (8), 3259-3266.

(46) Vasanthacharya, N.; Ganguly, P.; Goodenough, J.; Rao, C. Valence states and magnetic properties of $LaNi_{1-x}Mn_xO_3$ (for $0 \leqslant x \leqslant 0.2$ and $x = 0.5$). *J. Phys. C: Solid State Phys.* **1984**, *17* (15), 2745.

(47) Thenuwara, A. C.; Cerkez, E. B.; Shumlas, S. L.; Attanayake, N. H.; McKendry, I. G.; Frazer, L.; Borguet, E.; Kang, Q.; Remsing, R. C.; Klein, M. L.; et al. Nickel Confined in the Interlayer Region of Birnessite: an Active Electrocatalyst for Water Oxidation. *Angew. Chem. Int. Ed.* **2016**, *55* (35), 10381-10385.

(48) Wang, X.-D.; Cao, Y.; Teng, Y.; Chen, H.-Y.; Xu, Y.-F.; Kuang, D.-B. Large-Area Synthesis of a Ni_2P Honeycomb Electrode for Highly Efficient Water Splitting. *ACS Appl. Mater. Interfaces.* **2017**, *9* (38), 32812-32819.

For Table of Contents Only